

Characterization of Plastic Deformation Behavior of a Thermally Aged Duplex Stainless Steel

Gang Liu, Yanli Wang, Shilei Li, Hailong Zhang, and Xitao Wang

(Submitted March 22, 2016; in revised form March 18, 2017; published online May 1, 2017)

In situ tensile tests at room temperature have been conducted on a duplex stainless steel (DSS) thermally aged at 400 °C for 10,000 h to investigate both the plastic deformation mechanisms and the effect of long-term thermal aging on crack initiation. After thermal aging, the ultimate tensile strength of the DSS increases and the plasticity significantly decreases. The fracture morphology changes from ductile fracture with shallow dimples to a mixture of cleavages in ferrite and tearing in austenite. Electron backscattered diffraction (EBSD) technique has been used to determine the crystallographic orientations of austenite and ferrite grains on three areas deformed differently. The EBSD analysis results indicate that high strain occurs near grain boundaries and phase boundaries. The localized strain incompatibility is considered to be responsible for high stress concentration and crack initiation. The long-term thermal aging affect on the crack initiation and the cleavage cracks are found to be initiated in aged ferrite grains.

Keywords crack initiation, duplex stainless steel, EBSD, TEM, tensile deformation, thermal aging

1. Introduction

Duplex stainless steels (DSS) have a good combination of high corrosion resistance and excellent mechanical properties (such as high strength and toughness) for their duplex structure of ferrite and austenite. However, this type of steel is susceptible to embrittlement during long-term service at 300–500 °C (Ref 1, 2). Up to now, a lot of publications have studied the properties of the thermally aged DSS, like fracture toughness, tensile strength (Ref 3, 4), fatigue resistance (Ref 5, 6) or corrosion resistance (Ref 7, 8). The elastic and plastic deformation behaviors of the ferrite and austenite phases exhibit a large anisotropy because of their different crystallographies (Ref 9, 10).

Several groups have studied the mechanical behavior of DSS during plastic deformation (Ref 11–13). Guo et al. (Ref 11) investigated both the plastic deformation mechanism and the effect of temperature on mechanical properties of DSS through in situ tensile tests at 25–750 °C. The in situ observations reveal that the plastic deformation firstly appears in soft austenite matrix and then emerges in ferrite grains. Voids tend to form at

the phase boundaries and then propagate to the austenite matrix. Serre et al. (Ref 12) found that the slip lines are easily distinguished between austenite and ferrite from their morphologies. Frécharde et al. (Ref 13) revealed that dislocations pile up against the phase boundaries in austenite and create a local stress concentration. As a result, some neighboring ferrite grains are sheared off.

There are two views on the crack initiation mechanism for the thermally aged DSS materials: (1) crack nucleation in the ferrite and (2) micro-crack initiation at phase boundaries or interfaces. Although numerous papers make an effort on the deformation behavior and the crack initiation mechanism, the crack initiation site for aged materials is still not clear.

On one hand, Hausilda et al. (Ref 14) and M'cirdi et al. (Ref 15) revealed by in situ observations that the cleavage crack nucleation initiates on highly deformed bands in the ferrite after long-term thermal aging. With the Charpy V-notch and CT test at room temperature, Seiichi et al. recognized that dimples and cleavage are typical fracture modes for aged CF8M duplex stainless steels, and a mixture of dimples, cleavage and grain boundary separation is the fracture mode for the steels aged at a higher temperature (Ref 2).

Devillers-Guerville et al. (Ref 16) also recognized that nucleation of cleavage cracks in the ferrite phase is the main damage mechanism for a cast duplex stainless steel containing about 20% ferrite that is aged at 400 °C. Li et al. (Ref 17) revealed that micro-cracks are observed in the aged ferrite near tensile fracture, and the hardened ferrite phases are fractured before the failure of the tensile sample. On the other hand, Kobayashi et al recognized that micro-cracks initiate at grain boundaries of aged ferrite phase and at ferrite/austenite interfaces in a thermally aged cast duplex stainless steel (Ref 18).

In the present study, we conduct an in situ tensile test of aged DSS to understand the mechanical properties of the steels and the crack initiation mechanism of the aged DSS at room temperature. The plastic deformation behavior is investigated by EBSD, TEM, and SEM. The role of ferrite-austenite phase boundaries is clarified. The fracture behavior is also studied.

Gang Liu, Yanli Wang, Shilei Li, and Hailong Zhang, State Key Laboratory for Advanced Metals and Materials, University of Science and Technology Beijing, Beijing 100083, China; and Xitao Wang, Collaborative Innovation Center of Steel Technology, University of Science and Technology Beijing, Beijing 100083, China. Contact e-mail: wangyl@ustb.edu.cn.

Table 1 The chemical composition of Z3CN20-09M DSS (wt.%)

Elements	Cr	Ni	Mn	Si	C	N	S	P	Cu	Co	Mo	Fe
Specimen	20.16	9.06	1.11	1.09	0.024	0.033	0.0039	0.023	0.031	0.026	0.26	Bal.
Ferrite	25.74	4.22	0.79	1.21	0.37	Bal.
Austenite	20.03	9.59	0.95	1.04	0.24	Bal.

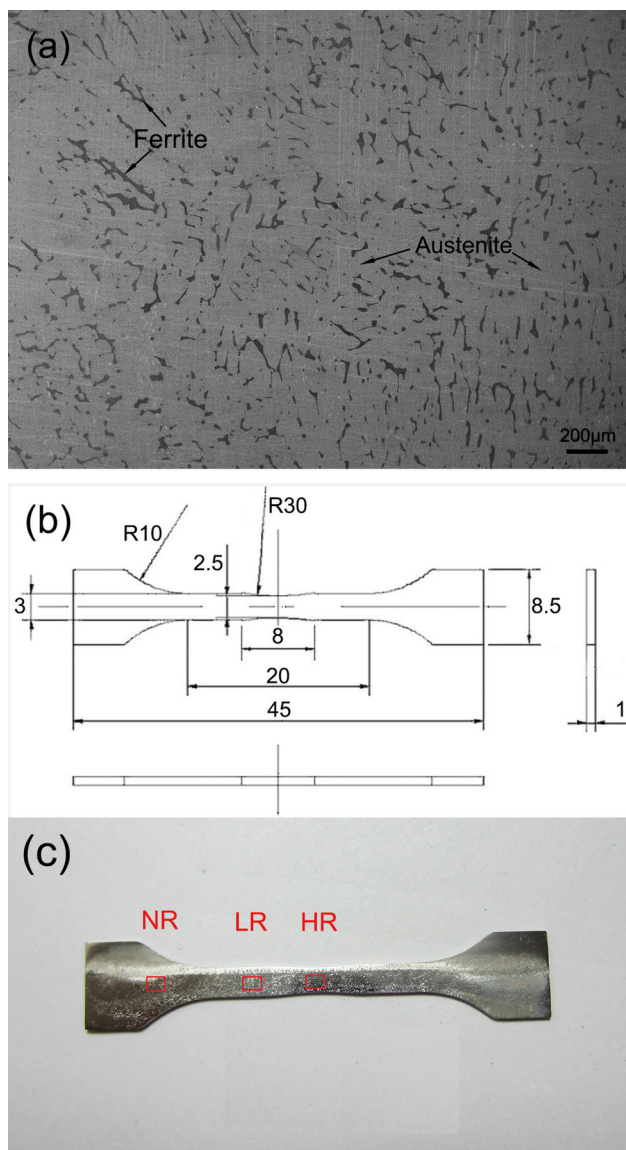


Fig. 1 (a) Electron backscattered map showing the microstructure of Z3CN20-09M DSS. Ferrite is distributed in the austenite matrix. (b) The schematic diagram of in situ tensile test sample (unit: mm). (c) Three different areas, NR: no deformation region, LR: low-strain region, HR: high-strain region

2. Material and Experimental Methods

The statically cast Z3CN20-09M DSS for pressurized water reactor coolant system piping is solution treated at 1100 °C for 8 h before water quenching, followed by further thermal aging

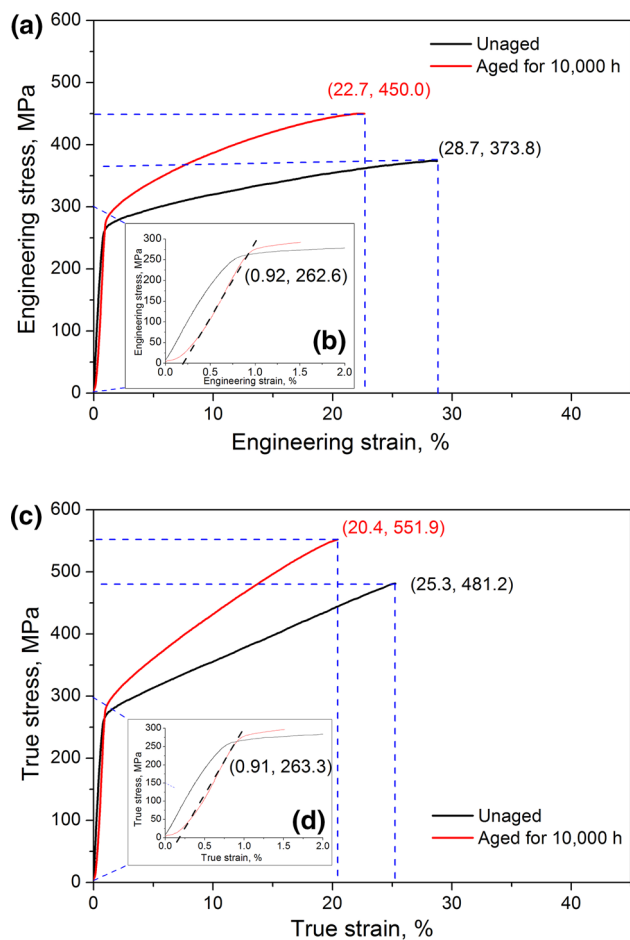


Fig. 2 Engineering stress-strain curves (a, b) and true stress-strain curves (c, d) of the duplex steels investigated

at 400 °C for as long as 10,000 h. The chemical compositions of the DSS with about 15% α -ferrite content are listed in Table 1. The electron backscattered map of the Z3CN20-09M DSS presents morphology of ferrite dendrites in the austenite matrix, as shown in Fig. 1(a).

Figure 1(b) presents the schematic diagram of in situ tensile samples, which have a gauge length of 20 mm and a cross-sectional area of 2.5 mm \times 1.0 mm. The length aligns along the tensile axis and three different areas are selected (each 1155 μ m \times 864 μ m in size). The three areas correspond to three different levels of strains, namely no deformation region (NR), low deformation region (LR), and high deformation region (HR), as shown in Fig. 1(c). The deformation features of the three areas mentioned above could qualitatively express the plastic deformation behavior during tensile test. For different stages of the tensile test, the deformation feature of the specimen central regions and the three areas mentioned above

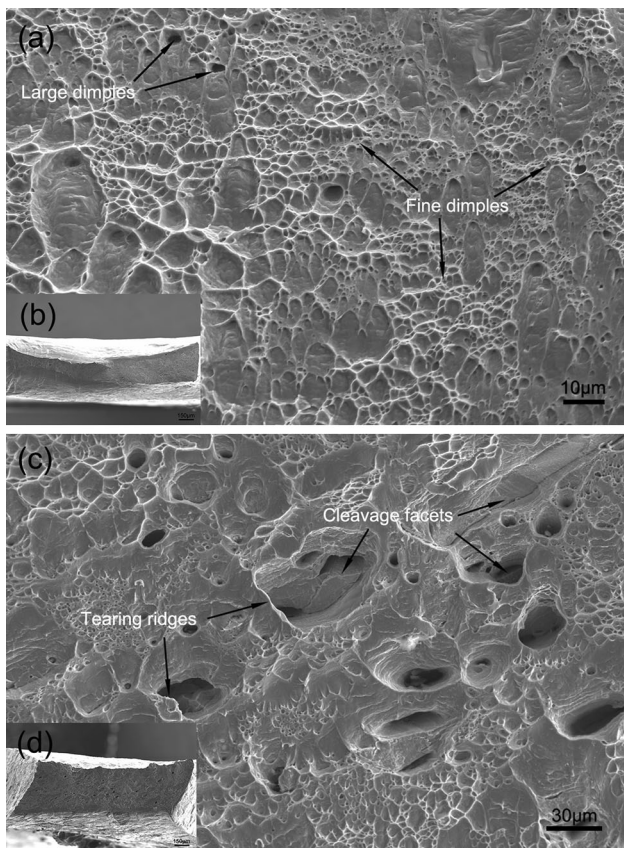


Fig. 3 The fracture SEM figures of in situ tensile sample (a, b) unaged and (c, d) aged for 10,000 h

shows little difference. Unfortunately, it is difficult to quantitatively achieve the crystallographic orientation analysis of the specimen central regions at different deformation stages. During the tensile test, surface characteristics of the specimen central regions at different deformation stages were characterized in situ by SEM. The crystallographic orientation analysis of the specimen central regions was carried out before and after the in situ tensile test. Before measurement, the specimens were mechanically grinded with silicon carbide paper from grade 400 to grade 2000, and then polished with diamond paste (1 and 0.25 mm). Finally, they were electro-polished using a 5% perchloric acid (HClO_4)-95% ethanol ($\text{C}_2\text{H}_5\text{OH}$) solution to remove the hardened layer, with the voltage of 20 V for 30 s.

Tensile tests were performed on a servo-hydraulic testing system installed inside the chamber of a scanning electron microscope (SEM, Shimadzu Corporation, Japan). The compositions of ferrite and austenite in DSS were detected by an electron probe micro-analyzer (EPMA, JEOL JXA 8100, Japan). Electron backscattered diffraction (EBSD) analysis

was carried out on a SEM (Zeiss Auriga, Germany), equipped with EBSD instrument (HKL, Oxford, England). Tensile fracture and surface characteristics were characterized by SEM. Microstructures in regions deformed differently for both unaged and aged samples were observed by a field emission transmission electron microscope (HRTEM, FEI Tecnai F20-ST, Netherlands) operated at 200 kV.

3. Results and Discussion

3.1 Effect of Aging on Tensile Properties

Typical uniaxial tensile stress-strain curves of unaged and aged samples are shown in Fig. 2. The ultimate tensile strength increases from 373.8 MPa of unaged material to 450.0 MPa of 10,000 h aged material, and the plasticity quantified by elongation percentage significantly decreases from 28.7% of unaged material to 22.7% of 10,000 h aged material. The zoomed view of the stress-strain curves reveals that the yield strength is not strongly affected by aging time, as shown in Fig. 2(b) and (d). In the elastic and yielding stage, multiple slip bands and dislocation pinning are mostly formed in austenite phase (Ref 12). At this stage, thermal aging has a small influence on yield strength. However, after yielding and work hardening of the soft austenite phase, sufficient stress is transferred to the hard ferrite phase to cause deformation, resulting in an increase in tensile strength. It is well known that the hardness of ferrite substantially increases with thermal aging time (Ref 19, 20). After long-term thermal aging, the pinned dislocations in ferrite and along ferrite-austenite boundaries create high stress concentration, and the tensile toughness decreases and the work hardening rate increases accordingly.

The tensile fracture morphologies of the unaged and aged specimens are shown in Fig. 3. For the unaged sample, the tensile fracture shows fine and homogeneous dimples, and both ferrite and austenite have good plasticities (Fig. 3a and b). After aging for 10,000 h, this material shows a mixed fracture mode of large dimples and tearing ridges in austenite and cleavage facets in ferrite (Fig. 3c and d).

The surface morphologies of the tensile sample central regions for the three different strains are also investigated by SEM, as shown in Fig. 4. The tensile axis is horizontal in these figures. It is clear that no slip line is found in the austenite matrix or in ferrite grains for both unaged and aged materials at 0% strain (Fig. 4a and b). When the tensile deformation develops at the yielding stage (strain at 0.91%), multiple slip bands and dislocation pinning are mostly found in austenite phase. As shown in Fig. 4(c) and (d), a lot of slip lines tend to propagate along the grain orientation and stop at phase boundaries in the austenite phase. In an FCC-structured metal, dislocations glide along one of four $\{111\}$ planes with three possible $\langle 110 \rangle$ directions in each plane. As a result, as many as 12 glide systems can be considered in austenite. However, a

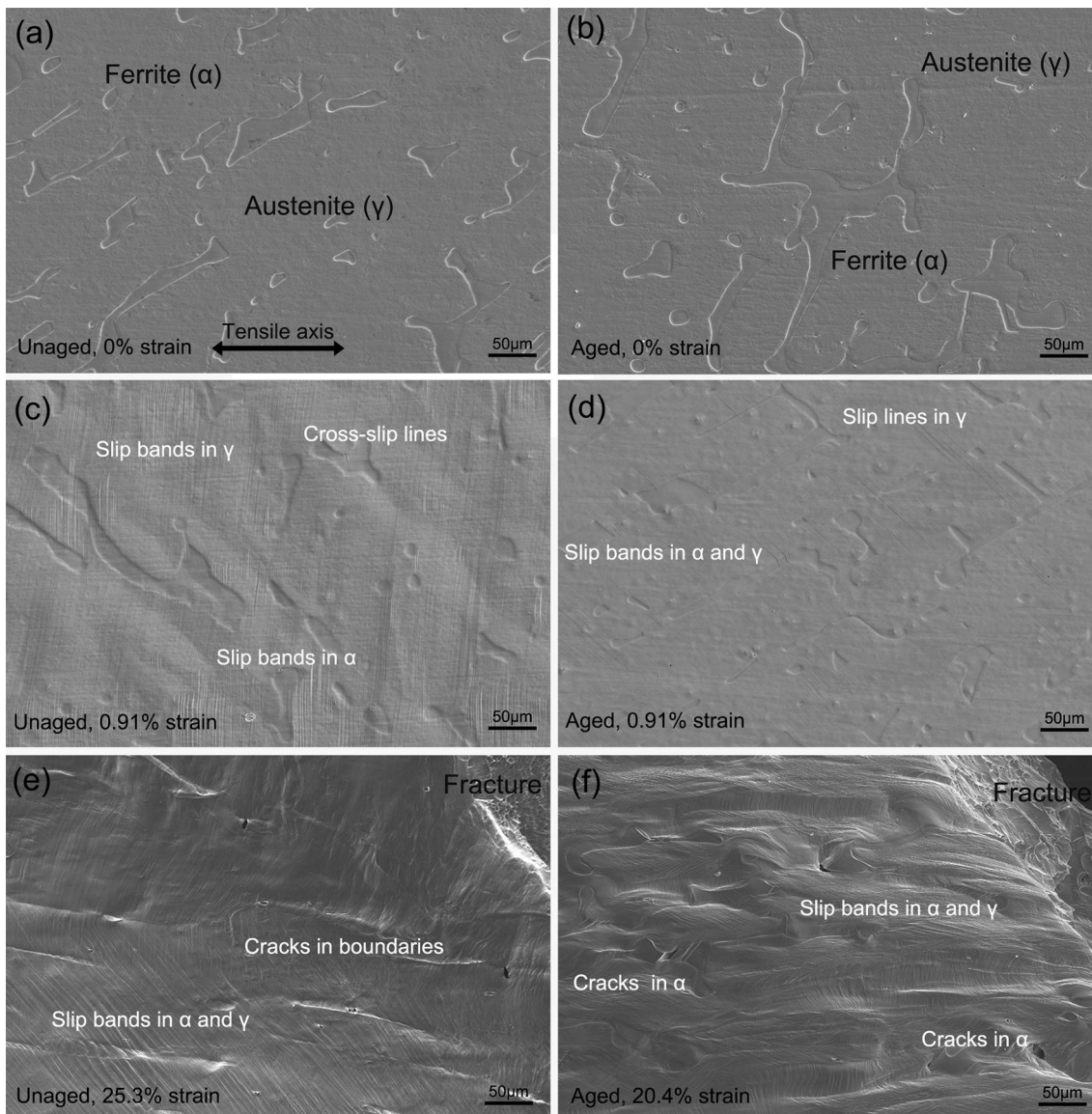


Fig. 4 SEM observations of in situ tensile sample central regions at three different strains: (a) unaged at 0%, (b) aged for 10,000 h at 0%, (c) unaged at 0.91%, (d) aged for 10,000 h at 0.91%, (e) unaged at 25.3%, and (f) aged for 10,000 h at 20.4%

few slip lines are found in some ferrite grains. It is well known that austenite phase with FCC structure has more opportunities to trigger slip system than ferrite phase with BCC structure during deformation (Ref 13). The plastic activity of austenite grains depends on their intrinsic characteristics of glide and orientation, whereas the plastic activity of ferrite grains are strongly influenced by their relative misorientation and the activity developed within the neighboring austenite grains (Ref 21, 22).

As the plastic deformation degree increases, extensive plastic deformation and multiple slip lines are observed in unaged ferrite and austenite grains, as shown in Fig. 4(e) (strain

at 25.3%). Cross-slips become easier in austenite phase. It is well known that multiple slip bands and cross-slip lines are firstly formed in austenite phase and these slip lines can pass through the phase boundaries to go into ferrite grains. Some cracks at ferrite-austenite phase boundaries are found in the unaged material, as shown in Fig. 4(e). However, more micro-cracks are observed in aged ferrite grains when the strain develops at 20.4%, as shown in Fig. 4(f). These micro-cracks near the tensile fracture of the long-term aged specimens correspond to the cavities in Fig. 3(c) and (d). After long-term thermal aging, the pinned dislocations in ferrite and along ferrite-austenite boundaries could lead to high stress concentration

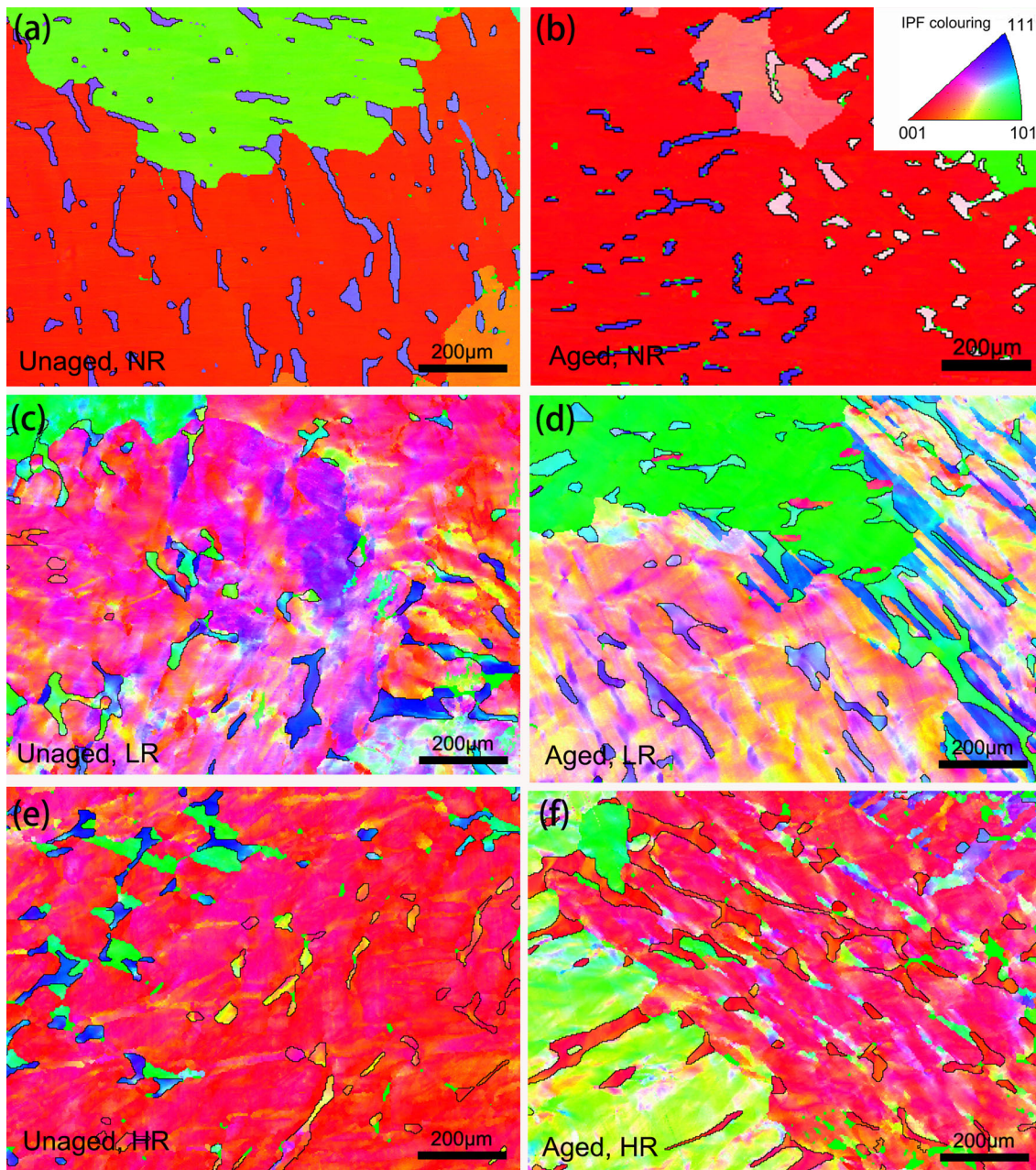


Fig. 5 EBSD orientation maps in three different deformation regions: (a) unaged at NR, (b) aged for 10,000 h at NR, (c) unaged at LR, (d) aged for 10,000 h at LR, (e) unaged at HR, and (f) aged for 10,000 h at HR; red: $\langle 001 \rangle$, blue: $\langle 111 \rangle$, green: $\langle 101 \rangle$ (Color figure online)

and produce deformation voids. These voids could cause the separation of the two phases and the tearing of surrounding austenite phases. Accordingly, the hardened and embrittled ferrite phase will fracture before the break of the tensile specimen.

3.2 Effect of Aging on Plastic Deformation Behavior

The EBSD orientation maps are used to characterize the change of microstructural features in the regions deformed differently, as presented in Fig. 5. In NR region, there is no obvious difference in either the grain orientation or the grain

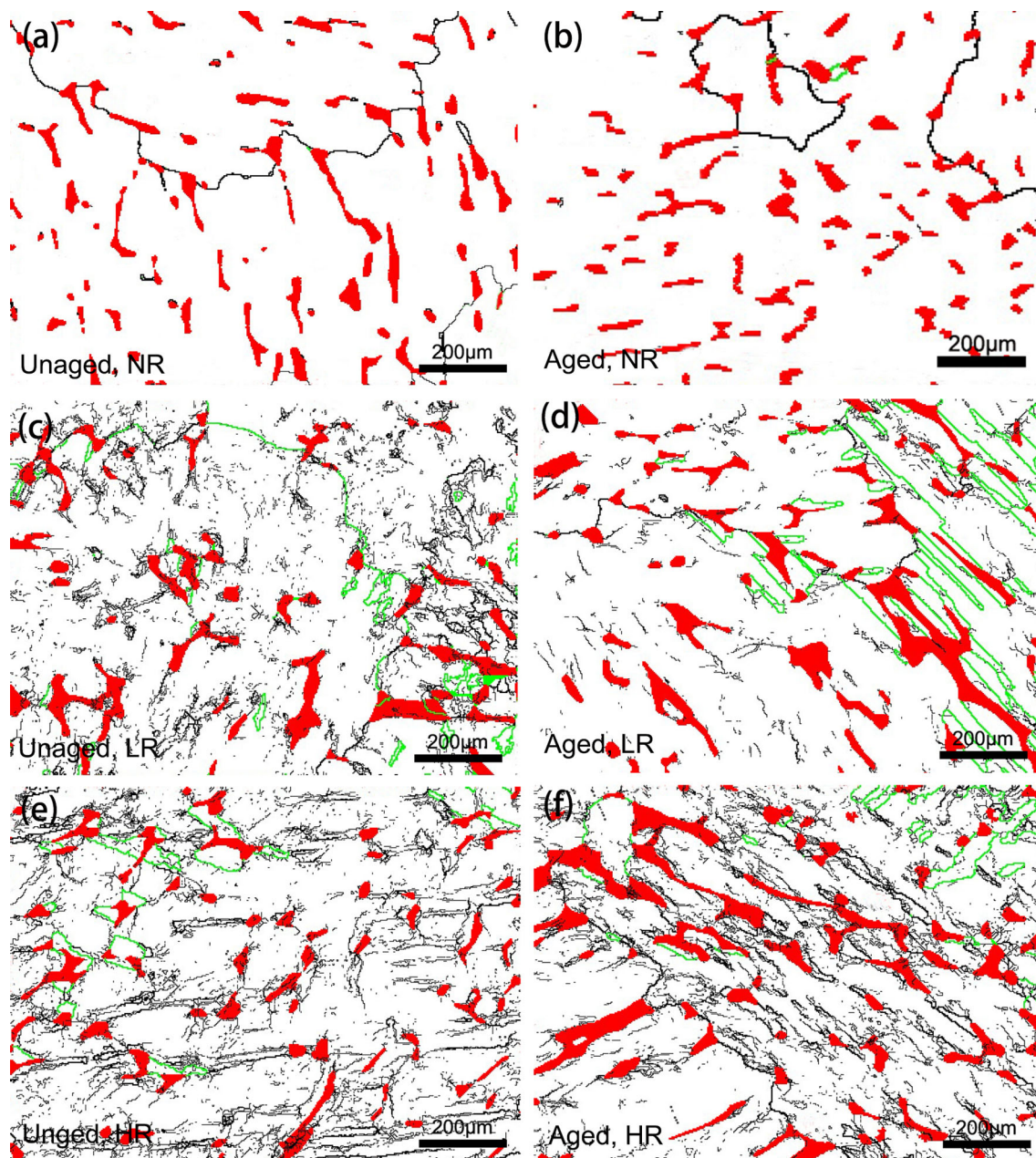


Fig. 6 Phase and grain boundary maps in three different deformation regions: (a) unaged at NR, (b) aged for 10,000 h at NR, (c) unaged at LR, (d) aged for 10,000 h at LR, (e) unaged at HR, and (f) aged for 10,000 h at HR; red areas: ferrite phase, fine black lines: 5° to 15° small misorientation, thick black lines: 15° - 45° intermediate misorientation, green lines: $>45^\circ$ large misorientation (Color figure online)

shape for both unaged and aged samples. With increasing strain, the variance in color, representing the development of the local misorientation, becomes more evident in ferrite and austenite grains. In HR area, the variance in overall color of certain grains is also clearly identified.

Figure 6 shows the phase and grain boundary maps in the three regions deformed differently. For each map, thin black

lines indicate low-angle boundaries ($5^\circ <$ misorientation angle $< 15^\circ$), thick black lines high-angle boundaries ($15^\circ <$ misorientation angle $< 45^\circ$), and thick green lines higher-angle boundaries ($45^\circ <$ misorientation angle). Ferrite and austenite phases are presented by red and blue colors, respectively. In NR region, there is no obvious difference between unaged and aged samples in the feature of both low-

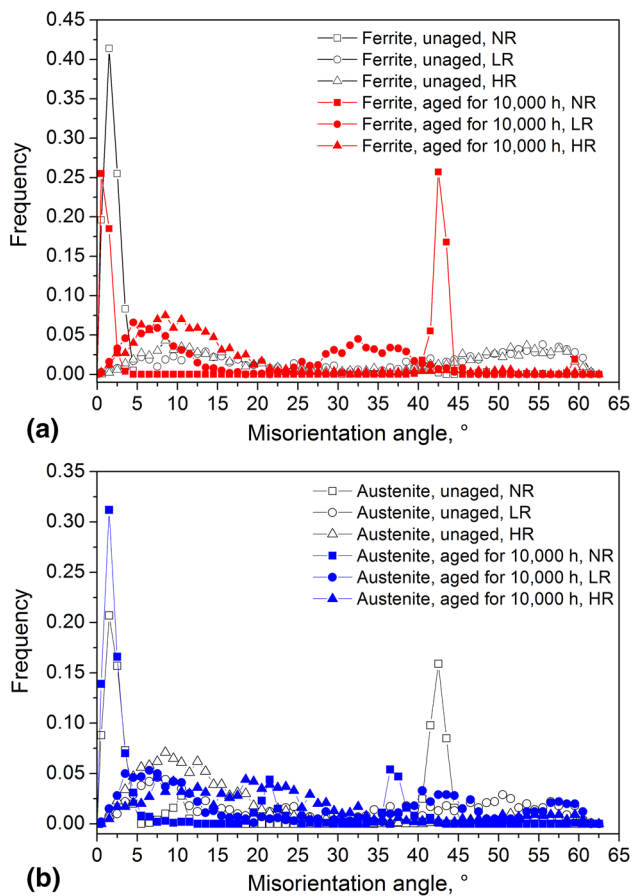


Fig. 7 The distribution of the misorientation angle in different deformation regions: (a) ferrite phase for unaged and aged samples and (b) austenite phase for unaged and aged materials

angle boundaries and other boundaries, as shown in Fig. 6(a) and (b). As the deformation degree increases, a large number of low-angle boundaries develop nearby the austenite grain boundaries or phase boundaries for the unaged materials, as shown in Fig. 6(c). At the same time, these low-angle boundaries in the interior of austenite grains correspond to the multiple slip bands and cross-slip lines in Fig. 4(c) and (d). Compared with unaged samples, more low-angle boundaries appear in ferrite grains for the thermally aged materials and a few high-angle boundaries (thick black lines) are also observed in a ferrite grain, as shown in Fig. 6(d). As deformation proceeds, the fraction of low-angle boundaries continuously increases in both austenite and ferrite phases, as shown in Fig. 6(e) and (f). A few higher-angle boundaries are clearly identified in some aged ferrite grains. However, there are more higher-angle boundaries in LR than in NR and HR regions for the unaged and aged austenite phases. These thick green lines are likely related to the development of the deformation twins in austenite phase (about 60°) or to the increase in the misorientation between neighboring austenite grains, as shown in Fig. 6(c) and (d).

Figure 7 shows the distribution of the misorientation angle in different deformation regions. In NR region, many low-angle boundaries (misorientation $< 5^\circ$) present in the ferrite and austenite grains. As the strain increases, the misorientation angle evolves differently between the ferrite and austenite phases. For the ferrite phase, the high-angle boundary ($5^\circ < \text{misorientation} < 15^\circ$) increase with increasing deformation degree. Meanwhile, the frequency of high-angle boundaries increases faster in the aged materials than in the unaged samples. For the ferrite phase, the frequency distribution of higher-angle boundaries has no obvious difference in the three deformation regions, as shown in Fig. 7(a). For the austenite phase, there are more higher-angle boundaries in LR than in NR and HR regions, as shown in Fig. 6 and 7(b).

Based on the distribution of misorientation angles across grain boundaries in the three different deformation regions, the strain contouring mappings are obtained from EBSD analysis of the unaged and aged specimens, as shown in Fig. 8. The yellow regions indicate high values of micro-strain. Phase boundaries and higher-angle boundaries (misorientation angle $> 45^\circ$) are indicated by red and black lines, respectively. In NR region, low values of micro-strain regions are dominant in all the ferrite and austenite grains, as shown in Fig. 8(a) and (b). As the deformation degree increases, a large number of high micro-strain regions develop nearby the austenite grain boundaries or phase boundaries for the unaged materials, as shown in Fig. 8(c). Compared with the aged samples, more yellow regions are observed near the austenite grain boundaries and phase boundaries for the unaged materials in LR region. In HR region, the yellow regions become homogeneous in both austenite and ferrite grains, as shown in Fig. 8(e) and (f). These micro-strain regions nearby austenite grain boundaries or phase boundaries correspond to the distribution of grain boundaries in Fig. 6. Due to the hardening of aged ferrite grains, cracks initiating at the phase boundaries have more opportunities to expand to ferrite grains.

Figure 9 indicates the distribution of strain values in different deformation regions of the tensile samples. For the ferrite phase, it is clear that the frequency of low-local strain areas (local misorientation $< 1^\circ$) decreases with increasing deformation degree. At the same time, the frequency of low-local strain areas decreases faster in the unaged samples than in the aged materials. In HR region, the frequency of high-local strain areas (local misorientation $> 2^\circ$) increases with increasing deformation degree for the unaged and aged samples, as shown in Fig. 9(a). With increasing deformation degree, the distribution of the local misorientation is almost the same in the austenite grains (see in Fig. 9b).

3.3 Effect of Aging on Microstructure

Figure 10 shows the TEM and HRTEM micrographs of ferrite and austenite phases in the unaged and aged materials before tensile deformation. For the unaged sample, a number of dislocations within ferrite and some stacking fault in austenite phase are found, as shown in Fig. 10(a); no precipitation is found, as shown in Fig. 10(b). The corresponding electron diffraction (ED) patterns of ferrite are also shown. After thermally aged at 400°C for 10,000 h, the morphology of aged

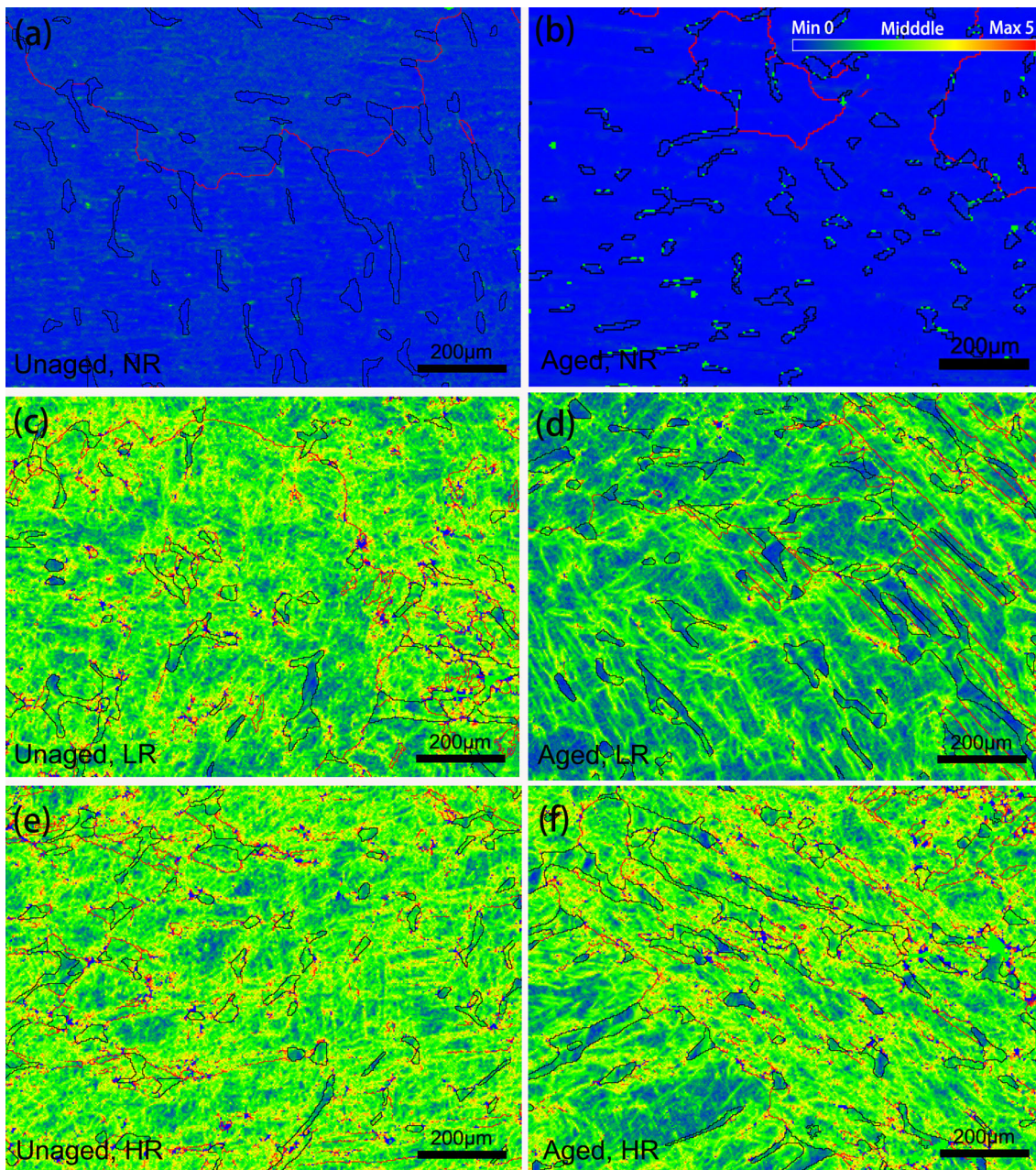
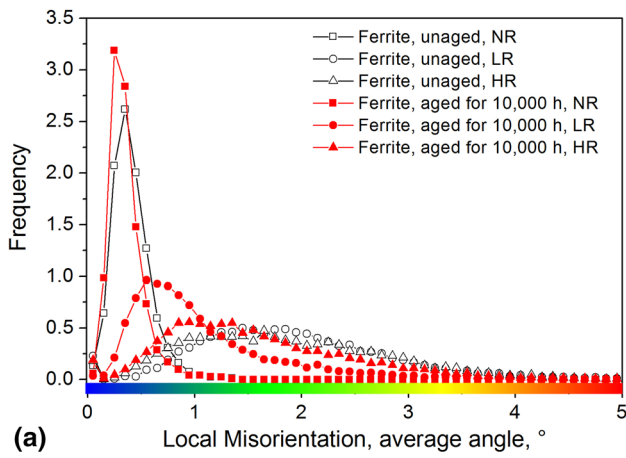


Fig. 8 Strain contouring mappings in three different deformation regions: (a) unaged at NR, (b) aged for 10,000 h at NR, (c) unaged at LR, (d) aged for 10,000 h at LR, (e) unaged at HR, and (f) aged for 10,000 h at HR; black lines: phase interface, red lines: $>45^\circ$ large misorientation. The yellow region in the map indicates high value of micro-strain (Color figure online)

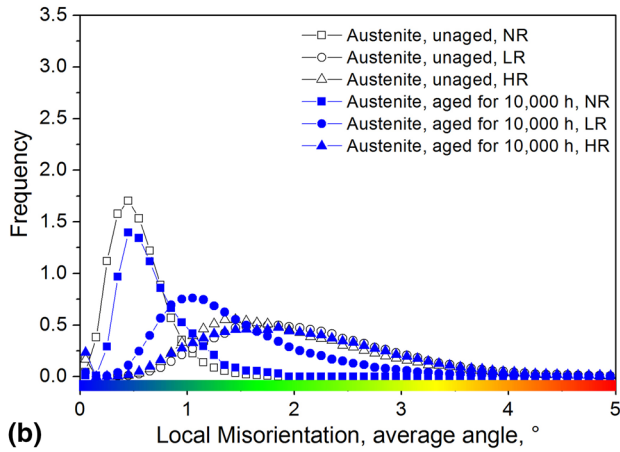
ferrite and austenite phase is observed, as shown in Fig. 10(c). Figure 11(d) shows the microstructure of the aged ferrite phase and precipitated particles. The precipitated particles are identified as G-phases, which agrees with those previously reported (Ref 23, 24). After long-term thermal aging, ferrite phases

decompose into Fe-rich α and Cr-enriched α' , indicated by the mottled contrast precipitates.

Figure 11 shows the microstructure of ferrite and austenite phases in the unaged and aged materials after tensile deformation. For the unaged sample, multiple dislocations pile-ups are



(a)



(b)

Fig. 9 The distribution of strain values in different deformation regions of tensile samples: (a) ferrite phase for unaged and aged samples and (b) austenite phase for unaged and aged materials

observed at phase boundaries, as shown in Fig. 11(a) and (b). It is well known that multiple dislocations and slip lines are firstly formed in austenite phase, as shown in Fig. 4. As the deformation proceeds, these dislocations along ferrite-austenite boundaries could pass through the phase boundaries to go into

ferrite grains. These pinned dislocations are considered to be responsible for high stress concentration and crack initiation. After long-term thermal aging, the pinning effect of spinodal decomposition precipitates and G-phase precipitates on dislocation movement is related to the degradation of deformation ability of ferrite, as shown in Fig. 11(c) and (d). Furthermore, the pinned dislocations in ferrite and along ferrite-austenite boundaries lead to high stress concentration and produce deformation voids (Fig. 3c and d). These voids could cause the separation of the two phases and the tearing of surrounding austenite phases. However, the blocking effect of α' phases and G-phase on dislocation movement is stronger than that of austenite grain boundaries or phase boundaries. Crack preferentially initiates in aged ferrite phase and deformation voids are formed after thermal aging, as indicated in Fig. 4(e) and (f).

4. Conclusions

The effect of long-term thermal aging on the microstructure and deformation behavior of duplex stainless steel was studied. The main conclusions are drawn as follows.

1. After long-term thermal aging, the ultimate tensile strength increases and the plasticity decreases significantly. The fracture pattern changes from ductile fracture with fine and deep dimples to a mixture of cleavage in ferrite and shallow dimples and tearing ridges in austenite.
2. After long-term thermal aging, the pinning effect of spinodal decomposition precipitates and G-phase precipitates on dislocation movement leads to the degradation of deformation ability of ferrite.
3. High stress concentration and crack initiation are observed near the grain boundaries and the phase boundaries for the unaged materials.
4. The blocking effect of α' phases and G-phase on dislocation movement is stronger than that of austenite grain boundaries or phase boundaries. Micro-cracks are primarily observed in ferrite phase for the aged materials.

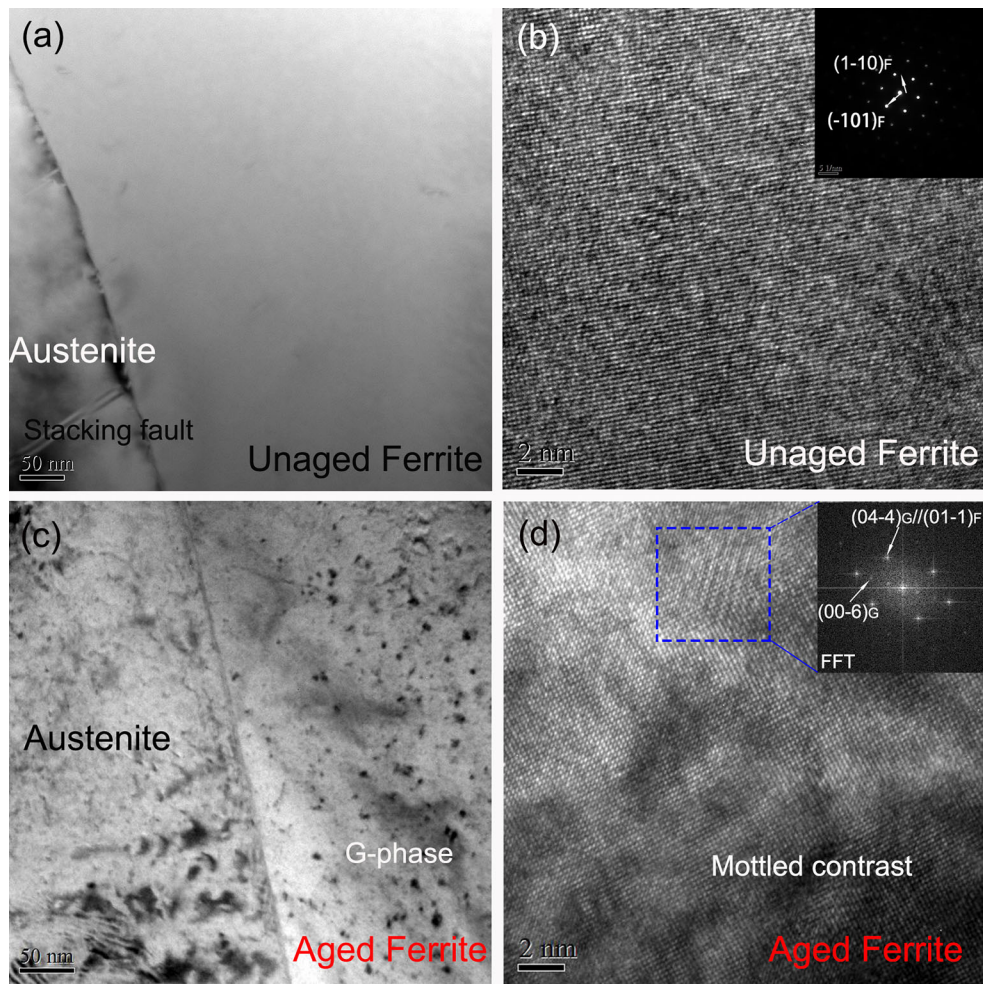


Fig. 10 TEM and HRTEM micrographs of ferrite before tensile deformation: the top right corner showing the corresponding ED patterns: (a, b) unaged and (c, d) aged for 10,000 h

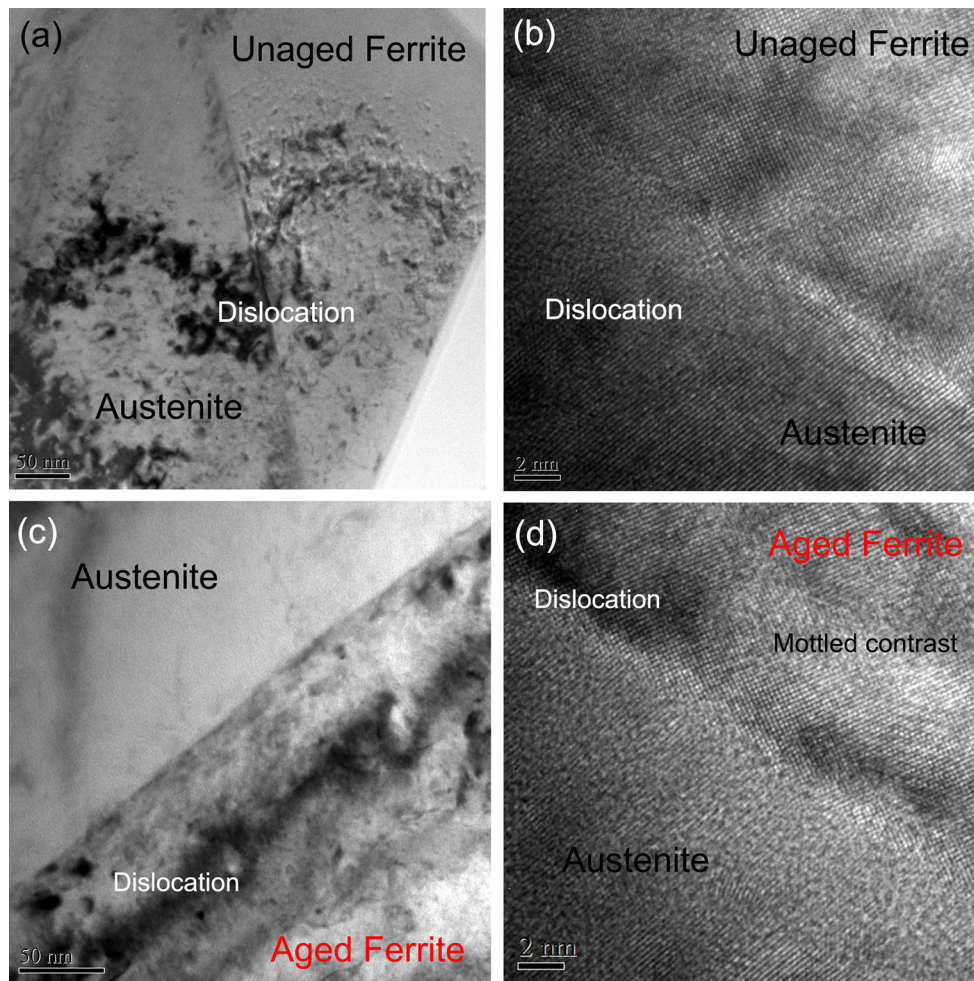


Fig. 11 TEM micrographs showing dislocations and phase boundaries in ferrite and austenite phases of specimens deformed differently: (a, b) deformation areas in the unaged material and (c, d) deformation regions in the material aged at 400 °C for 10,000 h

Acknowledgments

This work was financially supported by the National High-Tech Research and Development Program of China (863 Program) through Grant No. 2012AA03A507, the China Postdoctoral Science Foundation (2014M560043), the Fundamental Research Funds for the Central Universities (FRF-TP-14-046A1), and the State Key Lab for Advanced Metals and Materials (No. 2014Z-08 and 2016ZD-09).

References

1. H.M. Chung, Aging and Life Prediction of Cast Duplex Stainless Steel Components, *Int. J. Press. Vessels Pip.*, 1992, **50**, p 179–213
2. K. Seiichi, S. Naruo, and T. Genta, Microstructural Changes and Fracture Behavior of CF8M Duplex Stainless Steels After Long Term Aging, *Nucl. Eng. Des.*, 1997, **174**, p 273–285
3. M.D. Mathew, L.M. Lietzan, K.L. Murty, and V.N. Shah, Low Temperature Aging Embrittlement of CF-8 Stainless Steel, *Mater. Sci. Eng. A*, 1999, **269**, p 186–196
4. Y. Takuyo, O. Satoshi, and K. Hisashi, Mechanical Property and Microstructural Change by Thermal Aging of SCS14A Cast Duplex Stainless Steel, *J. Nucl. Mater.*, 2006, **350**, p 47–55
5. J.D. Kwon, S.W. Woo, Y.S. Lee, J.C. Park, and Y.W. Park, Effects of Thermal Aging on the Low Cycle Fatigue Behavior of Austenitic–Ferritic Duplex Cast Stainless Steel, *Nucl. Eng. Des.*, 2001, **206**, p 35–44
6. S. Hereñú, M. Sennour, M. Balbia, I. Alvarez-Armas, A. Thorel, and A.F. Armas, Influence of Dislocation Glide on the Spinodal Decomposition of Fatigued Duplex Stainless Steels, *Mater. Sci. Eng. A*, 2011, **528**, p 7636–7640
7. C.J. Park and H.S. Kwon, Effects of Aging at 475 °C on Corrosion Properties of Tungsten-Containing Duplex Stainless Steels, *Corros. Sci.*, 2002, **44**, p 2814–2830
8. F. Iacoviello, F. Casari, and S. Gialanella, Effect of “475 °C Embrittlement” on Duplex Stainless Steels Localized Corrosion Resistance, *Corros. Sci.*, 2005, **47**, p 909–922
9. R. Dakhlaoui, C. Brahama, and A. Baczmanski, Mechanical Properties of Phases in Austeno-Ferritic Duplex Stainless Steel—Surface Stresses Studied by X-ray Diffraction, *Mater. Sci. Eng. A*, 2007, **444**, p 6–17
10. N. Jia, R.L. Peng, G.C. Chai, S. Johansson, and Y.D. Wang, Direct Experimental Mapping of Micro-scale Deformation Heterogeneity in Duplex Stainless Steel, *Mater. Sci. Eng. A*, 2008, **491**, p 425–433
11. E.Y. Guo, M.Y. Wang, T. Jing, and N. Chawla, Temperature-Dependent Mechanical Properties of an Austenitic–Ferritic Stainless Steels Studied by In Situ Tensile Loading in a Scanning Electron Microscope (SEM), *Mater. Sci. Eng. A*, 2013, **580**, p 159–168
12. I. Serre, D. Salazar, and J.B. Vogt, Atomic Force Microscopy Investigation of Surface Relief in Individual Phases of Deformed Duplex Stainless Steel, *Mater. Sci. Eng. A*, 2008, **492**, p 428–433
13. S. Fréchar, F. Martin, C. Clément, and J. Cousty, AFM and EBSD Combined Studies of Plastic Deformation in a Duplex Steel, *Mater. Sci. Eng. A*, 2006, **418**, p 312–319
14. P. Haušilda, C. Berdina, P. Bompard, and N. Verdier, Ductile Fracture of Duplex Stainless Steel with Casting Defects, *Int. J. Pres. Vessels Pip.*, 2001, **78**, p 607–616

15. L. M'cirdi, J.L. Lebrun, K. Inal, and G. Barbier, Experimental Approach of a Crystallographic Cleavage Criterion in a Cast Aged Duplex Stainless Steel, *Acta Mater.*, 2001, **49**, p 3879–3887
16. L. Devillers-Guerville, J. Besson, and A. Pineau, Notch Fracture Toughness of a Cast Duplex Stainless Steel Modelling of Experimental Scatter and Size Effect, *Nucl. Eng. Des.*, 1997, **168**, p 211–225
17. S.L. Li, Y.L. Wang, S.X. Li, H.L. Zhang, F. Xue, and X.T. Wang, Microstructures and Mechanical Properties of Cast Austenite Stainless Steels After Long-Term Thermal Aging at Low Temperature, *Mater. Des.*, 2013, **50**, p 886–892
18. T. Kobayashi and D.A. Shockey, A Fractographic Investigation of Thermal Embrittlement in Cast Duplex Stainless Steel, *Phys. Metall. Mater. Sci.*, 1987, **18A**(11), p 1941–1949
19. V.H.C. de Albuquerque, E. de Macedo Silva, J. Pereira Leite et al., Spinodal Decomposition Mechanism Study on the Duplex Stainless Steel UNS S31803 Using Ultrasonic Speed Measurements, *Mater. Des.*, 2010, **31**, p 2147–2150
20. T. Goto, T. Naito, and T. Yamaoka, A Study on NDE Method of Thermal Aging of Cast Duplex Stainless Steels, *Nucl. Eng. Des.*, 1998, **182**, p 181–192
21. A. Gironès, P. Villechaise, A. Mateo, M. Anglada, and J. Méndez, EBSD Studies on the Influence of Texture on the Surface Damage Mechanisms Developed in Cyclically Loaded Aged Duplex Stainless Steels, *Mater. Sci. Eng. A*, 2004, **387–389**, p 516–521
22. C. Kahloun, R. Badji, B. Bacroix, and M. Bouabdallah, Contribution to Crystallographic Slip Assessment by Means of Topographic Measurements Achieved with Atomic Force Microscopy, *Mater. Charact.*, 2010, **61**, p 835–844
23. J.J. Shiao, C.H. Tsai, J.J. Kai, and J.H. Huang, Aging Embrittlement and Lattice Image Analysis in a Fe-Cr-Ni Duplex Stainless Steel Aged at 400 °C, *J. Nucl. Mater.*, 1994, **217**, p 269–278
24. S.L. Li, Y.L. Wang, X.T. Wang, and F. Xue, G-Phase Precipitation in Duplex Stainless Steels After Long-Term Thermal Aging A High-Resolution Transmission Electron Microscopy Study, *J. Nucl. Mater.*, 2014, **452**, p 382–388